Strain effects on thermal transport and anisotropy in thin-films of Si and Ge

Cameron J. Foss, and Zlatan Aksamija

View Online   Export Citation   CrossMark

ARTICLES YOU MAY BE INTERESTED IN

Nanoscale thermal transport
Journal of Applied Physics **93**, 793 (2003); https://doi.org/10.1063/1.1524305

Nanoscale thermal transport. II. 2003–2012
Applied Physics Reviews **1**, 011305 (2014); https://doi.org/10.1063/1.4832615

Phonon transport at interfaces between different phases of silicon and germanium
Journal of Applied Physics **121**, 025102 (2017); https://doi.org/10.1063/1.4973573

Strain effects on thermal transport and anisotropy in thin-films of Si and Ge

Cameron J. Foss and Zlatan Aksamija[a)]
Department of Electrical and Computer Engineering, University of Massachusetts-Amherst, Amherst, Massachusetts 01003-9292, USA

As dimensions of nanoelectronic devices become smaller, reaching a few nanometers in modern processors, CPU hot spots become increasingly more difficult to manage. Applying mechanical strain in nanostructures provides an additional tuning mechanism for both electronic band structures and phonon dispersions that is independent of other methods such as alloying and dimensional confinement. By breaking crystal symmetry, strain increases anisotropy. We present thermal conductivity calculations, performed in thin Si and Ge strained films, using first principles calculations of vibrational frequencies under biaxial strain, along with a phonon Boltzmann transport equation within the relaxation time approximation. We find that, while in-plane transport is not strongly dependent on strain, the cross-plane component of the thermal conductivity tensor shows a clear strain dependence, with up to 20% increase (decrease) at 4% compressive (tensile) strain in both Si and Ge. We also uncover that strain emphasizes the anisotropy between in-plane and cross-plane thermal conductivity across several orders of magnitude in film thickness. *Published by AIP Publishing.* [http://dx.doi.org/10.1063/1.4971269]

I. INTRODUCTION

Strain plays an important role in high performance silicon-based devices and has been shown to be a practical mechanism for tuning material (electrical, optical, and mechanical) properties of various nanostructured semiconductors. The crystalline similarities of silicon (Si) and germanium (Ge) have enabled a rich Si/SiGe heterostructure family, where the study of strain can be systematically approached[1] and applications in thermoelectrics,[2] optics,[3–5] and high-performance strained-Si CMOS have been realized.[6–9] As device dimensions push the limits into sub-20 nm scales, heat dissipation and CPU hot spots remain major points of interest.[10,11] The enhanced role of interactions between electrons and phonons in nanostructured systems makes studying the lattice thermal conductivity important for the understanding of heat transport phenomena in future device designs.[12,13]

Strain can affect the thermal properties of a material by shifting its vibrational (phonon) frequencies,[14–16] thereby changing its heat capacity, phonon group velocities, and phonon scattering rates, all of which contribute to the lattice thermal conductivity. It has been observed that hydrostatic compressive strain, corresponding to a decrease in molar volume, increases the thermal conductivity.[17,18] For non-hydrostatic strains in bulk materials, heat transport is dominated by heat capacity and internal scattering mechanisms that are independent of phonon velocity. When tensile uniaxial or biaxial strain is applied, heat capacity decreases and competes with increases in internal scattering, often resulting in a weak strain dependence.[19] On the other hand, heat transport in confined systems can become largely dominated by phonon interactions with the boundaries,[20] and the rate of boundary scattering is proportional to the phonon velocity in

the direction normal to the boundary.[21] Thus, we may expect to see a more definitive dependence on strain in nanostructured systems, due to the velocity-dependent scattering at rough boundaries.

Thermal conductivity of strained silicon-based nanostructures has been studied theoretically[17,22–24] and experimentally.[25] Xu and Li[22] studied cross-plane (CP) thermal transport in uniaxially and hydrostatically strained two-dimensional nanocomposites consisting of Si nanowires (NWs) embedded in Ge. They performed lattice dynamics calculations including strain, coupled to a phonon Boltzmann transport equation (pBTE) solver with diffuse NW boundaries, and found a large strain dependence in the cross-plane (along the embedded NWs) in $Si_{0.2}Ge_{0.8}$ nanocomposites under hydrostatic strain. Yang *et al.*[17] studied the strain effects on thermal conductivity in silicon NWs and thin films, as well as single-walled carbon nanotubes and two-dimensional graphene. They performed Equilibrium Molecular Dynamics (EMD) simulations to calculate the thermal conductivity (κ) which employs a numerical surface reconstruction method to account for surface interactions. Their results show that κ decreases monotonically from compressive to tensile strain in Si and diamond thin films and NWs.

Paul and Klimeck[23] studied the ballistic thermal transport in NWs under hydrostatic and uniaxial strains using a modified Valence Force Field (VFF) approach to calculate the phonon dispersion. For hydrostatic compressive/tensile strains, they found that thermal conductivity was unaffected. However, for uniaxial strain, a monotonic trend similar to Yang *et al.* was observed. Zhang and Wu performed MD studies of strained Si thin films[24] and also found a modest monotonic strain dependence for transport along the thin film. Murphy *et al.*[25] performed an experimental investigation into uniaxial strain in silicon NWs using a novel

a)Electronic mail: zlatana@engin.umass.edu

piezoelectric Raman Spectroscopy approach. Their findings support a weak strain dependence on heat transport in the direction along the NWs. Despite these studies, comparatively less attention has been devoted to the effect of biaxial strain on thermal transport in thin Si and Ge films, which may impact applications in strain-engineered silicon-on-insulator (sSOI)[26–28] and strained germanium-on-insulator (sGOI) nanomembrane devices,[29,30] as well as strained Si[2] and Si/Ge superlattice thermoelectrics.[31–33] Even less attention has been devoted to transport in the direction normal to the thin film/membrane (cross-plane direction), and the anisotropy between transport along and across the film/membrane.

In this paper, we augment the aforementioned studies with our calculations of both in-plane (IP) and cross-plane (CP) thermal conductivity, performed with the pBTE, focusing on Si and Ge thin films under both compressive and tensile biaxial strain and with film thickness varying across six orders of magnitude. The full phonon dispersion is calculated from first-principles of Si and Ge up to $\pm 4\%$ (tensile/compressive) biaxial strains. While our results confirm weak strain dependence in silicon and germanium thin films for IP thermal transport, we uncover a much stronger strain dependence in the CP direction. We provide an explanation on where from this strain-dependence discrepancy between IP and CP transport originates through our momentum-dependent boundary scattering model. In 20 nm films at room temperature, 4% strain results in a large $\sim 20\%$ variation in the CP conductivity, with tensile strain decreasing and compressive strain increasing the conductivity. Since IP conductivity remains relatively unaffected, we also observe increases (decreases) with tensile (compressive) strain in the significant anisotropy between IP and CP transport. Our results indicate that strain may be an effective tool for modulating the cross-plane thermal conductivity in thin-films for efficient heat removal from strained Si/SOI and Ge/GOI devices.

This paper is organized as follows: Sec. II will discuss components of heat transport and the details of our pBTE model. Sec. III will discuss the first-principles calculation and how strain affects the vibrational modes. Lastly, Sec. IV will discuss our findings on the anisotropic thermal transport in Si/Ge thin films with supporting plots showing group velocities, heat capacity, and the ratio between in-plane and cross-plane transport as a function of film thickness.

II. THEORY

A. Phonon BTE and intrinsic scattering mechanisms

The thermal properties of silicon nanostructures,[34] $Si_{1-x}Ge_x/Si_{1-y}Ge_y$ superlattices,[35] and other SiGe nanostructures[36] have been studied using a phonon Boltzmann transport model with a relaxation time approximation that incorporates intrinsic and extrinsic scattering mechanisms. We extend the use of this model and apply it to strained Si and Ge thin films. The temperature dependent thermal conductivity tensor can be obtained from a summation over all q-vectors $\boldsymbol{q}$ and phonon branches j as

$$\boldsymbol{K}^{\alpha\beta}(T) = k_B \sum_j \sum_{\boldsymbol{q}} C_j(\boldsymbol{q}, T)\tau_j(\boldsymbol{q})v_j^\alpha(\boldsymbol{q})v_j^\beta(\boldsymbol{q}). \quad (1)$$

where $C_j(\boldsymbol{q}, T)$ is the heat capacity per mode, k_B is the Boltzmann constant, $\tau_j(\boldsymbol{q})$ is the total relaxation time, and $v_j^\alpha(\boldsymbol{q})$ is the phonon velocity in the α Cartesian direction. The modal heat capacity can be represented as a function of temperature and q-vector

$$C_j(\boldsymbol{q}, T) = \left[\frac{\hbar\omega_j(\boldsymbol{q})}{kT}\right]^2 \frac{e^{\hbar\omega_j(\boldsymbol{q})/kT}}{\left[e^{\hbar\omega_j(\boldsymbol{q})/kT} - 1\right]^2}. \quad (2)$$

The conductivity tensor is diagonal and isotropic in bulk Si and Ge ($\boldsymbol{K}^{xx} = \boldsymbol{K}^{yy} = \boldsymbol{K}^{zz}$) due to cubic symmetry, but in nanostructures such as thin films, boundary scattering and strain can break this symmetry and cause anisotropy.[37] For this reason, the conductivity tensor in thin Si films has been shown to have different components in the IP and CP directions.[21]

Our model accounts for isotope (I), internal three-phonon normal (N) and umklapp (U) intrinsic scattering mechanisms. The relation between individual scattering mechanisms and the total intrinsic relaxation time $\tau_{j,int.}(\boldsymbol{q})$ follows:

$$\frac{1}{\tau_{j,int.}(\boldsymbol{q})} = \frac{1}{\tau_{j,N}(\boldsymbol{q})} + \frac{1}{\tau_{j,U}(\boldsymbol{q})} + \frac{1}{\tau_{j,I}(\boldsymbol{q})}. \quad (3)$$

The temperature driven transition between normal and umklapp scattering processes in bulk Si and Ge is modeled using a general method described by Slack et al.[38] and can be written in the following forms:

$$\tau_{j,N}^{-1}(\boldsymbol{q}) = \frac{\gamma_j^2}{M\bar{v}_j^3}\omega_j^2(\boldsymbol{q})Te^{-\Theta_j/3T} \quad (4)$$

and

$$\tau_{j,U}^{-1}(\boldsymbol{q}) = \frac{\hbar\gamma_j^2}{M\Theta_j\bar{v}_j^2}\omega_j^4(\boldsymbol{q})Te^{-\Theta_j/3T}, \quad (5)$$

where M is the atomic mass, γ_j is the Grüneisen parameter, $\bar{v}_j$ is the average phonon group velocity of branch j, and Θ_j is the Debye temperature per branch, discussed further in Sec. IV and calculated from Eq. (17). While these rates are based on an empirical model rather than calculated from first principles, they do not have any adjustable parameters: γ_j, v_j, and Θ_j are all calculated from the phonon dispersion[36] and are not adjustable. Their accuracy is sufficient for the purposes of this work, because our focus is on trends in strain dependence in nanostructures, such as thin films, where boundary scattering, described further in Section II B, is dominant. First principles calculations of anharmonic phonon-phonon scattering in Si found the same quadratic dependence of the normal rate, but a stronger frequency dependence of the umklapp rate, with either a cubic[39] or quartic[40] trend. The latter was found to better capture the middle part of the frequency spectrum, where most of the contribution arises from in thin films, while the former has been analytically shown to better capture the scattering rate of long-wavelength phonons. Because of our focus on thin films,

the quartic frequency dependence of umklapp rates is matched by our rates. When tensile (compressive) strain is applied, normal and umklapp scattering between acoustic branches, which are the primary contributors to heat flow, have been found to increase (decrease) with the amount of strain.

Scattering with isotopes is elastic; hence, it is related to the vibrational density of states, as described in the following equation:[41,42]

$$\tau_{j,I}^{-1}(\boldsymbol{q}) = \frac{\pi V_0}{6} \Gamma_{Si} \omega^2 D(\omega),\qquad(6)$$

where V_0 is the volume per atom, $D(\omega)$ is the vibrational density of states, and $\Gamma_S i = \sum_i f_i (1 - m_i/\bar{m})^2$, where f_i is the natural abundance of isotope i with mass m_i, and the average mass is $\bar{m} = \sum_i f_i m_i$. The energy-dependent vibrational density of states

$$D(\omega) = \sum_i \int \frac{d\boldsymbol{q}}{(2\pi)^3} \delta[\omega - \omega_j(\boldsymbol{q})]\qquad(7)$$

is calculated using the Brillouin zone integration method described by Gilat and Raubenheimer.[43]

B. Boundary roughness scattering in thin films

We use a boundary scattering model that determines the specularity of boundary collisions from the surface roughness and angle of phonon wave incidence. This factor describes the probability of a wave phonon reflecting at the boundary; otherwise, the phonon is scattered diffusely, provided it does not scatter internally before reaching the boundary by the intrinsic mechanisms described in Section II A. The specularity of a given collision is determined from the phonon momentum by $p(\boldsymbol{q}) = \exp(-4\Delta^2 q^2 cos^2 \Theta_B)$ where Δ is the rms surface roughness and Θ_B is the angle of incidence.

The relaxation time for boundary events can be written in the following way:

$$\tau_{j,B}^{-1}(\boldsymbol{q}) = \frac{v_j^\perp(\boldsymbol{q})}{H} \frac{F_p(\boldsymbol{q}, H)}{1 - \frac{\tau_{j,int}(\boldsymbol{q}) v_j^\perp(\boldsymbol{q})}{H} F_p(\boldsymbol{q}, H)}.\qquad(8)$$

The first term gives a rate determined by the velocity of each phonon and the thickness of the film and the second term determines the specularity of the wave and typically takes values between 0 and 1. The relaxation time for boundary scattering depends on intrinsic scattering via a differential equation which gives rise to a scaling factor

$$F_p(\boldsymbol{q}, H) = \frac{[1 - p(\boldsymbol{q})]\left(1 - \exp\left[\frac{-H}{\tau_{j,int}(\boldsymbol{q}) v_{j,\perp}(\boldsymbol{q})}\right]\right)}{1 - p(\boldsymbol{q}) \exp\left[\frac{-H}{\tau_{j,int}(\boldsymbol{q}) v_{j,\perp}(\boldsymbol{q})}\right]}.\qquad(9)$$

Here, $\tau_{j,int}(\boldsymbol{q})^{-1}$ is the total scattering rate due to intrinsic mechanisms given in Eq. (3). The total scattering rate in the presence of both intrinsic and boundary interactions is the combination $\tau_j(\boldsymbol{q})^{-1} = \tau_{j,int}(\boldsymbol{q})^{-1} + \tau_{j,B}(\boldsymbol{q})^{-1}$. For a more complete derivation of the momentum-dependent specularity

parameter, boundary scattering terms, and components to the steady-state pBTE in thin Si films and Si-Ge superlattices, we refer to earlier works by Aksamija and Knezevic.[21,35]

We can see in Eq. (8) that in thin films where the thickness H is less than the perpendicular component of the phonon mean free path (mfp) given by the product of the relaxation time due to intrinsic mechanisms $\tau_{j,int}(\boldsymbol{q})$ and the perpendicular component of the phonon group velocity vector $v_j^\perp(\boldsymbol{q})$, boundary roughness becomes the dominant scattering mechanism. The rate of boundary scattering depends strongly on the velocity perpendicular to the boundary. We can further analyze this dependence in the limiting case of completely diffuse boundaries (where specularity $p = 0$) and weak intrinsic scattering. Then Eq. (8) reduces to a simpler form $\tau_{j,B}^{-1}(\boldsymbol{q}) = 2v_j^\perp(\boldsymbol{q})/H$, which is interpreted as saying that, in this limit where boundary scattering is dominant, phonon lifetime simply equals the average time it takes to reach a boundary. Then the rate of scattering due to boundary roughness is directly proportional to the component of the phonon group velocity in the direction perpendicular to the boundary. Consequently, decreases (increases) in velocity due to strain result in an increasing (decreasing) relaxation time, less (more) boundary scattering, and larger (smaller) thermal conductivity, respectively.

We anticipate the thermal conductivity in thin films to be more dependent on strain for this reason, especially the component of the thermal conductivity tensor (Eq. (1)) in the CP direction perpendicular to the boundaries of the thin film. In this limit, where boundary scattering is dominant over intrinsic, the diagonal components of the thermal conductivity tensor further simplify to

$$\boldsymbol{K}^\parallel(T) = k_B \frac{H}{2} \sum_j \sum_{\boldsymbol{q}} C_j(\boldsymbol{q}, T) \left[v_j^\parallel(\boldsymbol{q})\right]^2 / v_j^\perp(\boldsymbol{q})\qquad(10)$$

for the IP (parallel to the film) direction and

$$\boldsymbol{K}^\perp(T) = k_B \frac{H}{2} \sum_j \sum_{\boldsymbol{q}} C_j(\boldsymbol{q}, T) v_j^\perp(\boldsymbol{q})\qquad(11)$$

for the CP (perpendicular to the film) direction. In this limit, we can see that the thermal conductivity is directly proportional to both the heat capacity and the corresponding component of the group velocity. Hence, we expect the CP thermal conductivity to be highly sensitive to changes in phonon velocity caused by strain. The anisotropy between the IP and CP components of the tensor also increases in this limit approximately in proportion to the square of the ratio between the corresponding velocity components,

$$\boldsymbol{K}^\parallel / \boldsymbol{K}^\perp \approx \sum_j \sum_{\boldsymbol{q}} [v_j^\parallel(\boldsymbol{q}) / v_j^\perp(\boldsymbol{q})]^2,\qquad(12)$$

leading to a large potential anisotropy in thin films under biaxial strain.

III. PHONON DISPERSION UNDER STRAIN

In order to fully capture the effects of strain, we have calculated the phonon dispersion of Si and Ge under

compressive and tensile biaxial strains using first-principles Density Functional Perturbation Theory (DFPT). All simulations are performed with the open-source software Quantum-ESPRESSO[44] (www.quantumespresso.org). Fundamental changes in the mechanical properties of a material can be deduced from observing the phonon dispersion relations. Biaxial strain is applied by fixing the lattice constant in the xy-plane and allowing the out-of-plane (z-plane) lattice constant to relax energetically. Naturally, biaxial strain breaks the cubic symmetry of the face-center cubic lattice.

After the system energy has been minimized, a final self-consistent field calculation is performed. We use a norm conserving pseudopotential that uses a direct-fit Von Barth-Car method with a Perdew-Zunger (LDA) exchange correlation for Si, and a norm conserving pseudopotential that uses a Goedecker-Hartwigsen-Hutter-Teter method also with a Perdew-Zunger (LDA) exchange correlation for Ge. A $4 \times 4 \times 4$ Monkhorst-Pack grid size with a $1 \times 1 \times 1$ offset was used with an energy cutoff for plane waves of 16 Ry for Si and 24 Ry for Ge. Conventional lattice constants were used for unstrained cases, 5.431 Å for Si and 5.658 Å for Ge with a convergence threshold of 10^{-9}. After the self-consistent calculation, a phonon calculation is done to obtain dynamical matrices in Fourier space on a $4 \times 4 \times 4$ grid and a convergence threshold of 10^{-16}. The dynamical matrices are then inverse Fourier transformed from which phonon frequencies are sampled on a dense grid of 33 200 (232 400) k-points.

In Fig. 1, we show the dispersions for silicon and germanium plotted along high-symmetry paths Γ-K-X-Γ-L-X-W-L. A clear increase in optical branch frequencies with compressive strain is seen, with the exception of −2% strain in germanium. For tensile strains, there is a clear decrease in optical phonon frequencies in either material. Similar trends can be seen in previous works on strain effects on phonon dispersions of materials.[15,16,45] Branch-wise phonon group velocities are calculated as the gradient of the dispersion, $v_j(\boldsymbol{q}) = \partial \omega_j(\boldsymbol{q})/\partial \boldsymbol{q}$, using a central difference method. Hence, the slope of the dispersion

curves represents the group velocity of phonons. Optical phonons have low velocities and are high in energy; thus, they act as energy storage and do not contribute greatly to heat flow. Conversely, acoustic phonons are high in velocity and are present at much lower temperatures; thus, acoustic phonons are the main contributors to thermal transport.

IV. RESULTS

A. Impact of strain on velocity and heat capacity

In order to see the energetic response to strain on phonon velocities, we have averaged the momentum-dependent group velocities ($v_j(\boldsymbol{q})$) obtained from central differences methods over the constant energy surface,

$$v_j^\alpha(\omega) = \frac{\int ||v_j^\alpha(\boldsymbol{q})||_2 \delta[\omega - \omega_j(\boldsymbol{q})]d\boldsymbol{q}}{\int \delta[\omega - \omega_j(\boldsymbol{q})]d\boldsymbol{q}}. \quad (13)$$

Acoustic phonons are the main contributors to heat flow and among them longitudinal acoustic (LA) phonons have the highest velocity. Eq. (13) returns the energy-resolved (averaged) velocities which can be plotted directly against the phonon energy spectrum (related to vibrational frequency through $E(\omega(\boldsymbol{q})) = \hbar\omega(\boldsymbol{q})$).

In Fig. 2, we plot the energy-resolved longitudinal acoustic phonon velocity for the applied strains. In either Si or Ge, high-velocity LA phonons increase with compressive strain and decrease with tensile strain. Since biaxial strain produces asymmetry between the xy-plane and z-plane, we want to distinguish between transport in the direction of strain (in the xy-plane) and perpendicular to the direction of strain (the cross-plane or z direction). The inset in Fig. 2 represents the norm of the branch-wise velocity vectors for the three acoustic branches (one LA and two transverse TA1 and TA2). The solid lines represent the IP (parallel) direction,
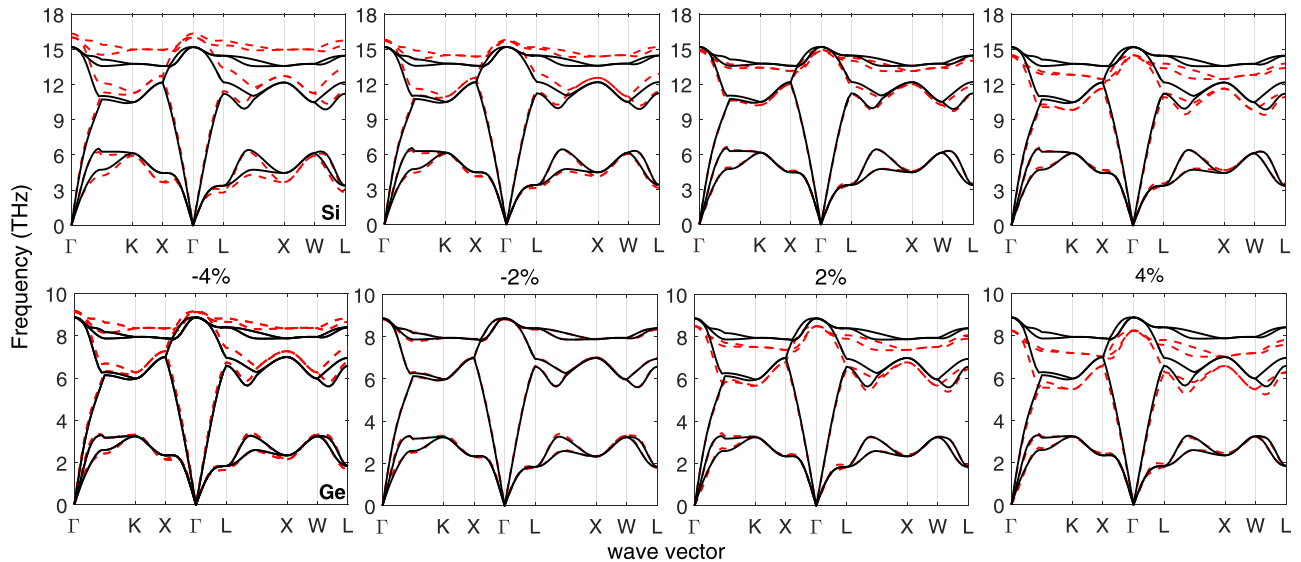

FIG. 1. The phonon dispersions of unstrained (solid black) and strained (dashed red) silicon (top) and germanium (bottom). The amount of strain increases from −4% to +4% from left to right. The six phonons branches from bottom to top are labeled TA1, TA2, LA, LO, TO1, and TO2 and represent transverse/longitudinal acoustic/optical phonons.
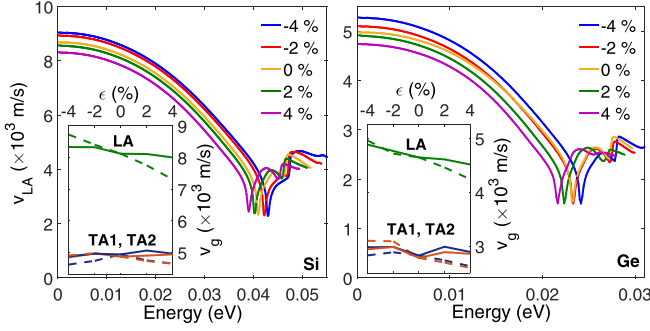
FIG. 2. The energy-resolved velocities of the longitudinal acoustic (LA) mode shown for various strain amounts. The inset shows the three acoustic modes (TA1, TA2, and LA) transport/parallel (solid) and boundary/perpendicular (dashed) components of the group velocity vectors as a function of strain.

whereas the dotted lines represent the CP (perpendicular) direction. A clear decreasing trend is seen in the CP LA mode velocities from compressive strain to tensile strain with about 10% variation at the highest strains, while IP velocities show less variation. Again, we do not plot the optical mode phonons here, because they generally have lower velocities and do not contribute greatly to heat transport in Si and Ge.

For clarity, the temperature dependent heat capacity per strain is presented in Fig. 3. The energy dependent volumetric specific heat is determined numerically by the following integral:

$$C_v(E, T) = \sum_{\boldsymbol{q}} \int_0^{\omega_D} \hbar\omega \frac{\partial f_{BE}}{\partial T} D(\omega) d\omega. \qquad (14)$$

The volumetric heat capacity defines how much thermal energy per unit volume of material is required to raise the temperature of the material by one degree. In bulk materials, heat capacity, together with internal scattering mechanisms, is intimately tied to thermal conductivity. At very low temperatures, thermal conductivity follows heat capacity as phonon scattering is comprised primarily of non-resistive normal processes and diffuse scattering at sample boundaries. At higher temperatures, heat capacity reaches a constant, and higher energy phonon collisions contribute to resistive umklapp processes, ultimately driving thermal conductivity lower with increasing temperature.
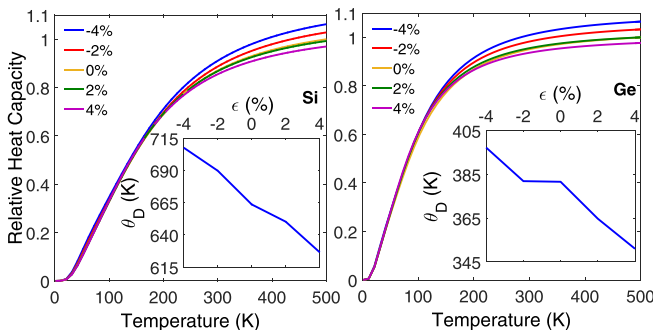

FIG. 3. The volumetric heat capacity is plotted relative to the unstrained heat capacity for silicon (left) and germanium (right) for different strains. The inset shows the calculated Debye temperature as a function of strain.

The low-T limit can be obtained by letting the upper limit of the integral $\omega_D = \Theta_D / T$, where Θ_D is the Debye temperature, go to infinity (as $T \ll \Theta_D$ in this limit), resulting in the approximate relationship

$$C_v(T) = \frac{12\pi^4 N k_B}{5\Theta_D^3} T^3. \qquad (15)$$

The high-T limit ($T \gg \Theta_D$) behavior of heat capacity can be analyzed in the Einstein model for phonon energies; in it, all phonons are treated as harmonic oscillators vibrating at frequency ω_0. Then the DOS becomes a delta function centered at ω_0—i.e., $D(\omega) = \delta(\omega - \omega_0)$. This simplification allows one to perform the integral in Eq. (14) and find the following expression:

$$C_v = \frac{6k_B}{V_{cell}}. \qquad (16)$$

Hence, variations seen in the high-temperature limit of the heat capacity are inversely related to variations in the unit cell volume with applied strain. In Fig. 3, we can see an increase (decrease) in the heat capacity obtained from Eq. (14) resulting from compressive (tensile) biaxial strain, respectively.

The inset in Fig. 3 shows similar trends for the strain-dependent Debye temperature, with the exception of −2% strain in Ge. We calculate the Debye temperature by averaging the phonon energy per branch over the density of states function, $g_j(w) = \sum_j \delta[\omega - \omega_j(\boldsymbol{q})]$. When the Brillouin zone sampling is dense, the summation can be replaced by an integral and we can calculate the Debye temperature as

$$\Theta_j^2 = \frac{5\hbar^2}{3k_B^2} \frac{\int \omega^2 g_j(\omega) d\omega}{\int g_j(\omega) d\omega}. \qquad (17)$$

A decreasing trend can be seen clearly moving from compressive to tensile strain in both Si and Ge.

B. Impact of strain on thermal conductivity

We have calculated the in-plane (κ_{IP}) and cross-plane (κ_{CP}) thermal conductivities of finite-volumed thin-films of strained silicon and germanium from 0 to 500 K. A surface rms roughness height (Δ) of 0.45 nm is used as a typical value in calculating the boundary scattering with roughened surfaces. The corresponding lattice orientations for the IP and CP directions are [100] and [001], respectively. Due to lattice symmetry, the [100] direction and the [010] direction are virtually identical in the unstrained and biaxially strained materials. The thermal conductivities are presented in Fig. 4, where the IP conductivity is in good agreement with previous theoretical and experimental studies on silicon-on-insulator samples.[21] We note that, similar to previous studies on silicon, an anisotropy (κ_{IP}/κ_{CP}) of a factor of 2 is observed for the room-temperature IP and CP conductivity due to boundary scattering. We extend these observations to thin-films of germanium, where a similar IP/CP anisotropy factor of approximately 1.8 is found.
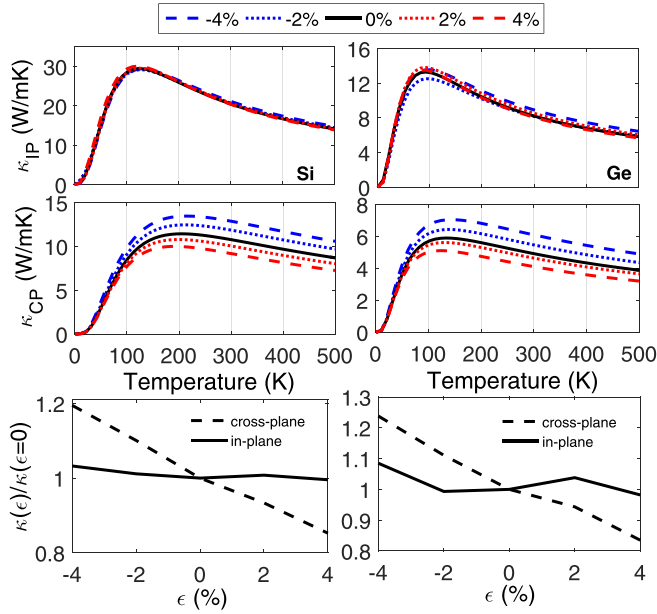
FIG. 4. The in-plane (top) and cross-plane (middle) thermal conductivities for 20 nm thick silicon (left) and germanium (right) thin-films with 0.45 nm surface roughness from 0 to 500 K. Strained materials are represented by blue (compressive) and red (tensile) dotted and dashed lines. (bottom) Change in thermal conductivity relative to the unstrained case as a function of strain for a 20 nm thin film with surface roughness 0.45 nm at 300 K, showing significant strain dependence of cross-plain conductivity.
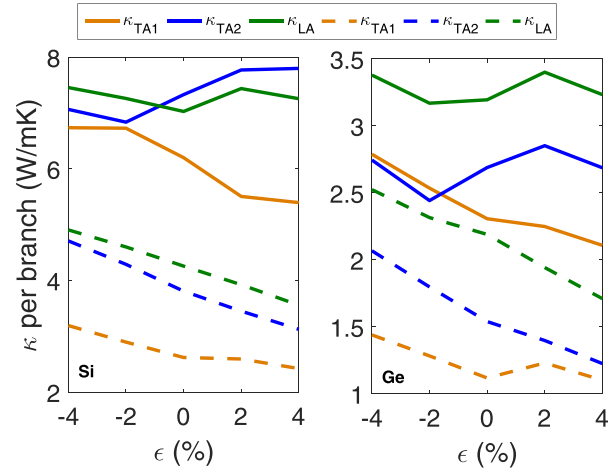

FIG. 5. The branch-wise contribution to IP (solid lines) and CP (dash lines) thermal conductivities of the acoustic phonon modes at room temperature as functions of strain. While the IP TA2 and LA mode contributions show no definitive trend, the IP TA1 and all acoustic CP modes monotonically decrease from compressive to tensile strain.

The strain dependence for κ_{IP} is seen to be moderate for both Si and Ge. However, for κ_{CP} at temperatures above approximately 100 K compressive (tensile) strain can be seen to strongly increase (decrease) the overall conductivity. To better illustrate the strain dependence, the bottom panel in Fig. 4 shows the percent change in $\kappa_{IP,CP}$ as a function of applied strain at room-temperature. We see a clear decreasing trend from a maximum boost of ~20% in Si (~25% in Ge) at 4% compressive strain to a decrease of ~15% in Si (~16% in Ge) in the CP conductivity at 4% tensile strain, while the IP conductivity remains relatively unchanged with variations <5% in Si (<10% in Ge) compared to the unstrained material. We note that our results are in agreement with prior theoretical[22] and experimental[25] studies supporting weak IP strain dependence and a stronger CP strain dependence. We can understand these trends based on Eqs. (10) and (11): the IP conductivity is driven more by phonons with large IP components of their group velocity. Such phonons interact less with boundary roughness, which is dependent on the CP velocity. In addition, heat capacity is also decreasing with tensile strain; taken together, tensile strain decreases heat capacity and IP velocity in the numerator of Eq. (10) and also decreases the CP velocity; hence, resulting in less boundary scattering, and the two trends cancel.

In contrast, CP transport depends only on the CP component of phonon velocity (Eq. (11)); so, phonons having larger CP velocity (directed into the boundary) contribute more to the CP transport and they also encounter more boundary scattering. Hence, as tensile strain reduces both the CP velocity and heat capacity, the two trends add and result in a much more pronounced strain modulation than the IP conductivity. In Fig. 5, the room-temperature IP and CP

conductivities presented in Fig. 4 are broken down into their acoustic mode contributions. Regarding the strain dependence of each acoustic mode, the TA2 and LA phonon modes for IP transport show no definitive trend, while the TA1 mode for IP and all acoustic modes for CP transport monotonically decrease from compressive to tensile strain. Collectively, for IP transport, the variations due to strain in the acoustic mode contributions lead to very little change in the total conductivity. On the other hand, since all acoustic modes show similar strain dependence, their collective contribution to CP transport reveals a clear increase (decrease) with compressive (tensile) strain in the total conductivity.

In addition, strain, inherently promotes anisotropic transport by breaking lattice symmetry between the direction(s) of the applied strain and the direction(s) perpendicular to the applied strain direction. To further probe the effects that strain has on the anisotropy between IP and CP transport, we have calculated the room-temperature thermal conductivity over several orders of magnitude of film thickness; the results are presented in Fig. 6. The right end of the horizontal axis represents a bulk like material, where the left end represents thin-films with thickness approaching nanometer lengths. As expected, anisotropy in unstrained Si or Ge goes to one at the bulk limit.

As the thickness of the film becomes smaller and boundary roughness scattering begins to play a stronger role, we can see a clear increase in the anisotropy in the unstrained materials, in agreement with Eq. (12). The anisotropy between IP and CP thermal conductivity gradually increases with decreasing thickness reaching a peak value of 3 (~2.4) at 2 nm for unstrained Si (Ge) and that tensile (compressive) strain increases (decreases) this ratio at low thicknesses. As shown earlier in Fig. 4, only the CP conductivity shows a pronounced strain dependence; hence, the anisotropy ratio κ_{IP}/κ_{CP} shows an inverse relationship to κ_{CP}, increasing with tensile strains and decreasing for compressive strains.

We note that our model has been previously validated against experimental data on supported Si films down to
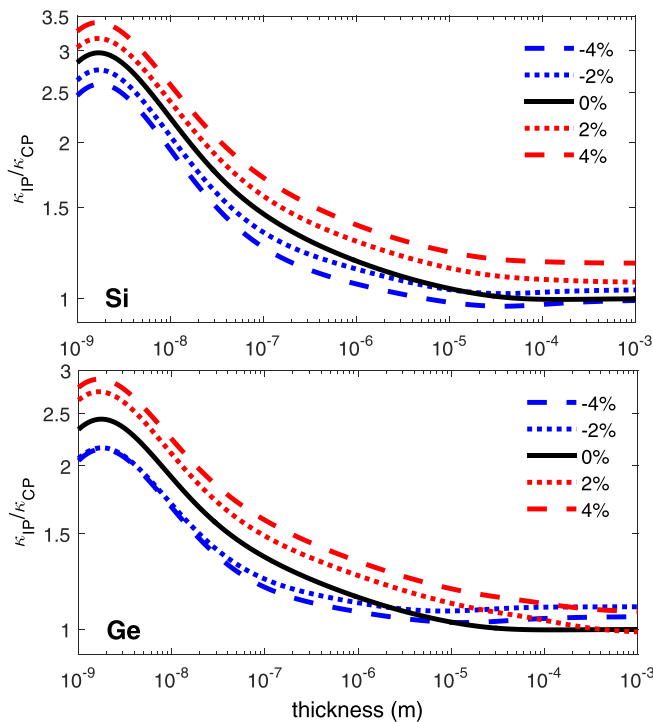
FIG. 6. The ratio between room-temperature in-plane and cross-plane thermal conductivity as a function of film thickness. The unstrained case (black) converges to one as expected when the thickness approaches the mean-free-path of phonons. Compressive strain (blue) and tensile strain (red) cause anisotropy even at thickness comparable to the bulk phonon mean-free-path.

20 nm thickness;[21] below this value, phonon confinement effects may alter the phonon velocities,[46] reducing thermal conductivity in the IP direction. The phonon confinement is counterbalanced by a reduction in the phase space available for scattering, which results in a reduced anharmonic phonon-phonon scattering rates,[47] so that the thermal conductivity of thin films below 13 nm is still dominated largely by boundary scattering and matches closely the predictions, based on bulk lattice dynamics.[48] Prasher et al.[49] have shown that the heat capacity is also altered in ultrathin nanostructures (NWs) below a certain critical diameter. Based on the dominant phonon model, they relate this critical diameter to the dominant phonon wavelength,[31,50,51] which is in the 1 to 10 nm range in Si.[52–54] Therefore, we consider the trends that we observe in Fig. 6, approximately below 10–13 nm, including the peak in anisotropy at 2 nm, to be a qualitative indicator of the trends, while the strain dependence of the CP thermal conductivity holds across a broad range of thicknesses approximately up to the phonon mean-free-path, or so long as boundary scattering is dominant.

V. CONCLUSIONS

We have analyzed the strain effects on the in-plane (IP) and cross-plane (CP) lattice thermal transport in thin films of Si and Ge. We employ the phonon Boltzmann transport equation under the relaxation time approximation, while accounting for anharmonic three-phonon scattering and isotope scattering. The phonon dispersion and group velocities are calculated from DFPT simulations in order to capture the impact of strain on the vibrational frequencies and group velocities. We use the Boltzmann transport formalism with momentum and roughness-dependent specularity coefficient to determine the probability of phonon scattering from the atomically rough boundaries in thin films. We find that strain affects phonon dispersion and creates the anisotropy between IP and CP group velocities. Boundary roughness scattering, combined with the change in phonon velocities, results in a large strain-induced variation of CP thermal conductivity, while the IP thermal conductivity, being less dominated by boundaries, does not strongly depend on strain. Ultimately, this strain dependence results in a larger anisotropy between IP and CP thermal transport. Our results indicate that heat removal from strained thin film devices can be improved by compressive strain because compressive strain increases the CP heat flow up to 20%. We conclude that strain engineering, while having modest impact in bulk or thick films, can be a an effective way to modulate the thermal conductivity in Si and Ge nanostructures in the direction perpendicular to their boundaries.

[1]D. J. Paul, Semicond. Sci. Technol. **19**, R75 (2004).
[2]N. F. Hinsche, I. Mertig, and P. Zahn, J. Phys.: Condens. Matter **23**, 295502 (2011).
[3]Y.-H. Kuo, Y. K. Lee, Y. Ge, S. Ren, J. E. Roth, T. I. Kamins, D. A. B. Miller, and J. S. Harris, Nature **437**, 1334 (2005).
[4]S. B. Samavedam, M. T. Currie, T. A. Langdo, and E. A. Fitzgerald, Appl. Phys. Lett. **73**, 2125 (1998).
[5]B. Schuppert, J. Schmidtchen, A. Splett, U. Fischer, T. Zinke, R. Moosburger, and K. Petermann, J. Lightwave Technol. **14**, 2311 (1996).
[6]M. V. Fischetti and S. E. Laux, J. Appl. Phys. **80**, 2234 (1996).
[7]M. V. Fischetti, Z. Ren, P. M. Solomon, M. Yang, and K. Rim, J. Appl. Phys. **94**, 1079 (2003).
[8]M. L. Lee, E. A. Fitzgerald, M. T. Bulsara, M. T. Currie, and A. Lochtefeld, J. Appl. Phys. **97**, 011101 (2005).
[9]I. Lauer and D. A. Antoniadis, IEEE Electron Device Lett. **26**, 314 (2005).
[10]D. G. Cahill, W. K. Ford, K. E. Goodson, G. D. Mahan, A. Majumdar, H. J. Maris, R. Merlin, and S. R. Phillipot, J. Appl. Phys. **93**, 793 (2003).
[11]D. G. Cahill, P. V. Braun, G. Chen, D. R. Clarke, S. Fan, K. E. Goodson, P. Keblinski, W. P. King, G. D. Mahan, A. Majumdar, H. J. Maris, S. R. Phillpot, E. Pop, and L. Shi, Appl. Phys. Rev. **1**, 011305 (2014).
[12]E. Pop, S. Sinha, and K. Goodson, Proc. IEEE **94**, 1587–1601 (2006).
[13]J. Zhou, B. Liao, and G. Chen, Semicond. Sci. Technol. **31**, 043001 (2016).
[14]J. Zi, K. Zhang, and X. Xie, Phys. Rev. B **45**, 9447 (1992).
[15]A. Qteish and E. Molinari, Phys. Rev. B **42**, 7090 (1990).
[16]Z. Sui and I. P. Herman, Phys. Rev. B **48**, 17938 (1993).
[17]X. Li, K. Maute, M. L. Dunn, and R. Yang, Phys. Rev. B **81**, 245318 (2010).
[18]R. G. Ross, P. Andersson, B. Sundqvist, and G. Backstrom, Rep. Prog. Phys. **47**, 1347 (1984).
[19]J. S. Jin, J. Mech. Sci. Technol. **27**, 2885 (2013).
[20]M. Asheghi, Y. K. Leung, S. S. Wong, and K. E. Goodson, Appl. Phys. Lett. **71**, 1798 (1997).
[21]Z. Aksamija and I. Knezevic, Phys. Rev. B **82**, 045319 (2010).
[22]Y. Xu and G. Li, J. Appl. Phys. **106**, 114302 (2009).
[23]A. Paul and G. Klimeck, Appl. Phys. Lett. **99**, 083115 (2011).
[24]X. Zhang and G. Wu, J. Nanomater. **2016**, 4984230.
[25]K. F. Murphy, B. Piccione, M. B. Zanjani, J. R. Lukes, and D. S. Gianola, Nano Lett. **14**, 3785 (2014).
[26]I. Aberg, C. N. Chleirigh, and J. L. Hoyt, IEEE Trans. Electron Devices **53**, 1021 (2006).
[27]C. Euaruksakul, Z. W. Li, F. Zheng, F. J. Himpsel, C. S. Ritz, B. Tanto, D. E. Savage, X. S. Liu, and M. G. Lagally, Phys. Rev. Lett. **101**, 147403 (2008).
[28]S.-Y. Kim, S.-Y. Choi, W. S. Hwang, and B. J. Cho, Sci. Rep. **6**, 29354 (2016).
[29]J. Snchez-Prez, C. Boztug, F. Chen, F. F. Sudradjat, D. M. Paskiewicz, R. Jacobson, M. G. Lagally, and R. Paiella, Proc. Natl. Acad. Sci. U.S.A. **108**, 18893 (2011).

[30]J. R. Jain, A. Hryciw, T. M. Baer, D. A. B. Miller, M. L. Brongersma, and R. T. Howe, Nat. Photonics **6**, 398 (2012).

[31]G. Chen, Phys. Rev. B **57**, 14958 (1998).

[32]T. Koga, X. Sun, S. B. Cronin, and M. S. Dresselhaus, Appl. Phys. Lett. **75**, 2438 (1999).

[33]M. Huang, C. S. Ritz, B. Novakovic, D. Yu, Y. Zhang, F. Flack, D. E. Savage, P. G. Evans, I. Knezevic, F. Liu, and M. G. Lagally, ACS Nano **3**, 721 (2009).

[34]Z. Aksamija and I. Knezevic, J. Comput. Electron. **9**, 173 (2010).

[35]Z. Aksamija and I. Knezevic, Phys. Rev. B **88**, 155318 (2013).

[36]M. Upadhyaya, S. N. Khatami, and Z. Aksamija, J. Mater. Res. **30**, 2649 (2015).

[37]A. K. McCurdy, H. J. Maris, and C. Elbaum, Phys. Rev. B **2**, 4077 (1970).

[38]D. T. Morelli, J. P. Heremans, and G. A. Slack, Phys. Rev. B **66**, 195304 (2002).

[39]K. Esfarjani, G. Chen, and H. T. Stokes, Phys. Rev. B **84**, 085204 (2011).

[40]A. Ward and D. A. Broido, Phys. Rev. B **81**, 085205 (2010).

[41]S.-I. Tamura, Phys. Rev. B **27**, 858 (1983).

[42]H. J. Maris, Phys. Rev. B **41**, 9736 (1990).

[43]G. Gilat and L. J. Raubenheimer, Phys. Rev. **144**, 390 (1966).

[44]P. Giannozzi, S. Baroni, N. Bonini, M. Calandra, R. Car, C. Cavazzoni, D. Ceresoli, G. Chiarotti, M. Cococcioni, I. Dabo, A. Dal Corso, S. Fabris, G. Fratesi, S. de Gironcoli, R. Gebauer, U. Gerstmann, C. Gougoussis, A. Kokalj, M. Lazzeri, L. Martin-Samos, N. Marzari, F. Mauri, R. Mazzarello, S. Paolini, A. Pasquarello, L. Paulatto, C. Sbraccia, S. Scandolo, G. Sclauzero, A. P. Seitsonen, A. Smogunov, P. Umari, and R. M. Wentzcovitch, J. Phys.: Condens. Matter **21**, 395502 (2009).

[45]R. Eryiğit and I. P. Herman, Phys. Rev. B **53**, 7775 (1996).

[46]J. Cuffe, E. Chvez, A. Shchepetov, P.-O. Chapuis, E. H. E. Boudouti, F. Alzina, T. Kehoe, J. Gomis-Bresco, D. Dudek, Y. Pennec, B. Djafari-Rouhani, M. Prunnila, J. Ahopelto, and C. M. S. Torres, Nano Lett. **12**, 3569 (2012).

[47]J. Cuffe, O. Ristow, E. Chávez, A. Shchepetov, P.-O. Chapuis, F. Alzina, M. Hettich, M. Prunnila, J. Ahopelto, T. Dekorsy, and C. M. Sotomayor Torres, Phys. Rev. Lett. **110**, 095503 (2013).

[48]X. Wang and B. Huang, Sci. Rep. **4**, 6399 (2014).

[49]R. Prasher, T. Tong, and A. Majumdar, Nano Lett. **8**, 99 (2008).

[50]G. Chen, J. Heat Transfer **119**, 220 (1997).

[51]S. Volz, J. Ordonez-Miranda, A. Shchepetov, M. Prunnila, J. Ahopelto, T. Pezeril, G. Vaudel, V. Gusev, P. Ruello, E. M. Weig, M. Schubert, M. Hettich, M. Grossman, T. Dekorsy, F. Alzina, B. Graczykowski, E. Chavez-Angel, J. Sebastian Reparaz, M. R. Wagner, C. M. Sotomayor-Torres, S. Xiong, S. Neogi, and D. Donadio, Eur. Phys. J. B **89**, 15 (2016).

[52]A. A. Balandin, J. Nanosci. Nanotechnol. **5**, 1015 (2005).

[53]A. S. Henry and G. Chen, J. Comput. Theor. Nanosci. **5**, 1 (2008).

[54]A. Malhotra and M. Maldovan, Sci. Rep. **6**, 25818 (2016).